Particle simulation study of collisionless driven reconnection in a sheared magnetic field

Ritoku Horiuchi and Tetsuya Sato
Theory and Computer Simulation Center, National Institute for Fusion Science, Nagoya 464-01, Japan

(Received 9 July 1996; accepted 21 October 1996)

Nonlinear development of collisionless driven reconnection and the consequent energy conversion process between the field and particles in a sheared magnetic field are investigated by means of a two-and-one-half-dimensional particle simulation. Magnetic reconnection takes place in two steps irrespective of a longitudinal magnetic field, but the growth rate of the reconnection field varies in proportion to the **E×B** drift velocity at an input boundary. It is clearly observed that the triggering mechanism of collisionless driven reconnection for the fast growing phase changes from an electron meandering dominance in a weak longitudinal field to an electron inertia dominance in a strong field. The electron acceleration and heating take place in the reconnection area under the influence of reconnection electric field, while the electron energy is converted to the ion energy through the action of an electrostatic (ambipolar) field excited by magnetic compression in the downstream. It is also found that, in the presence of a longitudinal magnetic field, the electron acceleration by the reconnection field takes place effectively and the generated force-free current is maintained for a long period while forming an asymmetric spatial profile of current layer. © *1997 American Institute of Physics.* [S1070-664X(97)00302-9]

I. INTRODUCTION

Driven magnetic reconnection[1] in a collisionless plasma, ''collisionless driven reconnection,'' is an important process in considering energetically active phenomena observed in a high temperature, rarefied plasma such as the solar corona,[2] geomagnetic tails,[3] laboratory plasmas,[4,5] fusion plasmas,[6] and so on. It is well-known that driven magnetic reconnection can lead to fast energy conversion from the field energy to the particle energy as well as a topological change of magnetic field in a collisionless plasma. If a current-carrying particle is lost from a current layer, an electric field is induced so as to accelerate a particle along the equilibrium current and compensate it for the momentum loss. This electric field also plays a role in changing the topology of magnetic field, i.e., magnetic field reconnection. Magnetic reconnection, however, cannot take place in an ideal magnetohydrodynamic (MHD) plasma because the magnetic field is frozen in a plasma. This means that the nonideal effect, which breaks the frozen-in condition and leads to the generation of an electric field, is needed for triggering magnetic reconnection in a plasma.

Because a charged particle has a finite mass and a finite temperature, it executes a complex thermal motion with a finite orbit amplitude in a sheared magnetic field. Therefore, the frozen-in condition of the magnetic field is not applicable to microscopic scale phenomena associated with the motion of charged particles, even for a collisionless plasma. Collisionless reconnection has been studied by using theoretical analyses,[7–13] particle simulation,[14–19] and fluid simulation.[20,21] Two types of mechanisms leading to the generation of a reconnection electric field in a collisionless plasma have so far been considered in relation to such a kinetic effect. The first one is a spontaneous excitation of the electric field caused by momentum loss of current carrying particles through a nonideal effect such as wave–particle interaction[22] or collisionless tearing instability.[8–14,17,18] Another mechanism is due to field penetration[23] when the current layer is compressed by an external driving source. An electric field, which is induced in the MHD region outside the current layer by the plasma flow moving across the magnetic field, can penetrate into the current layer through a particle kinetic effect when the current layer is compressed as thin as a characteristic spatial scale of a particle kinetic effect.

In a two-dimensional system there exist two types of particle kinetic effects which are responsible for the decoupling of the magnetic field from the particle motion in a collisionless plasma. One is the particle inertia effect, which becomes significant in a spatial scale comparable to collisionless skin depth.[16,20,21] The other is the particle orbit effect, which becomes effective in a characteristic spatial scale of particle thermal motion which is called a meandering motion.[12,19,24,25] Horiuchi and Sato[19] demonstrated two-dimensional particle simulation of collisionless driven reconnection for the case where the system is subjected to an external driving flow and there is no longitudinal magnetic field at an initial stage. They showed that magnetic reconnection is triggered by the meandering orbit effect when the current layer is compressed as thin as an average orbit amplitude of meandering particles, and that it evolves temporarily in two steps in accordance with the formation of two current layers, the widths of which are characterized by the average orbit amplitude of the ion and electron meandering motions, respectively. Because thermal motion of a charged particle is strongly dependent on the topology of the magnetic field and its strength, it is expected that collisionless driven reconnection and the resulting energy conversion process are largely affected by adding a longitudinal magnetic field.

In this paper, we will give detailed discussions on the electron dynamics in a sheared magnetic field in order to

clarify the difference between the electron inertia effect and the electron thermal effect on collisionless driven reconnection. For this purpose we have developed the electromagnetic (EM) particle simulation code with higher temporal and spatial resolutions compared with the previous one.[19,26,27] The numerical scheme and the simulation model are described in Sec. II. We reveal several new features in collisionless driven reconnection in a sheared magnetic field. For example, the triggering mechanism of collisionless driven reconnection changes from the electron thermal effect in a weak longitudinal field to the electron inertia effect in a strong field. This phenomenon is related to the fact that an electron thermal motion becomes more strongly magnetized and its spatial scale decreases as a longitudinal field increases.

From the particle simulation we find that the ion energy increases twice as large as the electron energy through collisionless driven reconnection. The same phenomenon is observed in experimental plasmas[5,28] in which a MHD relaxation controlled by collisionless or collisional magnetic reconnection takes place. This phenomenon is considered to be associated with the generation of collisionless ion viscosity, which leads directly to the ion heating.[5,29] In order to clarify this process, we examine the energy conversion process between the EM field and the charged particles through collisionless driven reconnection. Consequently, it is found that the energy conversion is controlled by two important mechanisms, i.e., the electron acceleration and heating by the reconnection electric field in the vicinity of the reconnection point, and the energy conversion from electron energy to ion energy through the action of the electrostatic field excited in the downstream by magnetic compression. These simulation results are discussed in detail in Sec. III. Finally, a brief summary and discussions are given in Sec. IV.

II. SIMULATION MODEL

Let us study magnetic reconnection in a collisionless plasma by means of two-and-one-half dimensional particle simulation for the case where the system is subjected to an external driving flow. The physical quantities are assumed to be translationally symmetric in the z direction ($\partial/\partial z=0$). The basic equations to be solved are the equations of motion

$$\frac{d(\gamma_j \mathbf{v}_j)}{dt}=\frac{q_j}{m_J}\left(\mathbf{E}+\frac{\mathbf{v}_j}{c}\times\mathbf{B}\right), \tag{1}$$

$$\frac{d\mathbf{x}_j}{dt}=\mathbf{v}_j, \tag{2}$$

and the Maxwell equations

$$\frac{1}{c}\frac{\partial A_z}{\partial t}=-E_z, \tag{3}$$

$$\frac{1}{c}\frac{\partial B_z}{\partial t}=-\frac{\partial E_y}{\partial x}+\frac{\partial E_x}{\partial y}, \tag{4}$$

$$\frac{1}{c}\frac{\partial \mathbf{E}}{\partial t}=\nabla\times\mathbf{B}-4\pi\mathbf{j}, \tag{5}$$

$$\nabla\cdot\mathbf{E}=4\pi\rho, \tag{6}$$

where

$$B_x=\frac{\partial A_z}{\partial y},\quad B_y=-\frac{\partial A_z}{\partial x}. \tag{7}$$

A_z, $\mathbf{x}_j(t)$, $\mathbf{v}_J(t)$, m_J, and q_J are the z component of the vector potential, the position, the velocity, the rest mass, and the charge of the jth particle, and the relativistic γ factor of the jth particle is defined by

$$\gamma_j=1/\sqrt{1-(\mathbf{v}_J\cdot\mathbf{v}_j)/c^2}. \tag{8}$$

The current density $\mathbf{j}(\mathbf{x},\mathbf{t})$ and the charge density $\rho(\mathbf{x},t)$ are obtained by summing over all the particles, namely,

$$\mathbf{j}(\mathbf{x},\mathbf{t})=\sum_{j=1}^{N}\frac{q_j\mathbf{v}_j(t)}{c}S[\mathbf{x}-\mathbf{x}_j(t)], \tag{9}$$

$$\rho(\mathbf{x},t)=\sum_{j=1}^{N}q_j S[\mathbf{x}-\mathbf{x}_j(t)], \tag{10}$$

where N is the total number of particles and $S(\mathbf{x})$ is the form function of particles.[19,30]

As an initial condition we adopt a one-dimensional equilibrium with a sheared magnetic field as

$$\mathbf{B}(y)=[B_x(y),0,B_{z0}], \tag{11}$$

$$B_x(y)=B_0\tanh(y/L), \tag{12}$$

$$P(y)=B_0^2/8\pi\,\mathrm{sech}^2(y/L), \tag{13}$$

where B_{z0} is a constant and L is the scale height along the y axis. There is a magnetically neutral sheet along the mid-horizontal line ($y=0$) in the initial equilibrium for the case of $B_{z0}=0$. The vector potential A_z is set at zero along the mid-horizontal line at $t=0$. Let us assume that the initial particle distribution is given by a shifted Maxwellian with a spatially constant temperature and the average particle velocity is equal to the diamagnetic drift velocity. Then, the particle position and the particle velocity are determined from the pressure profile $P(y)$ and the current density $\mathbf{j}(\mathbf{x},0)$ $\{=[0,0,-B_0/(4\pi L)\mathrm{sech}^2(y/L)]\}$. Because both an ion and an electron are loaded at the same spatial position, there is no electric field in the initial profile.

In order to drive magnetic reconnection at the center of the simulation domain we adopt an input boundary condition[19,27] at the boundary of the y axis ($y=\pm y_b$) and a periodic boundary condition at the boundary of the x axis ($x=\pm x_b$). At the input boundary the y derivative of the magnetic field is equal to zero and the plasma is smoothly supplied with the $\mathbf{E}\times\mathbf{B}$ drift velocity into the simulation domain. These conditions indicate that the total number of charged particles increases monotonously with time. The driving electric field at the input boundary is determined so as to be always normal to both the magnetic field and the input flow velocity. The amplitude of driving electric field $E_{d0}(x,t)$ is taken to be zero at $t=0$ and gradually increases for $0<\omega_{pe}t<100$ (ω_{pe} is an average electron plasma frequency). After this period ($\omega_{pe}t>100$), $E_{d0}(x,t)$ is described by a symmetric constant profile[19] as

$$E_{d0}(x,t)=E_0(\epsilon_f+(1-\epsilon_f)\{\cos[\phi(x)]+1\}/2), \tag{14}$$

where

$$\phi(x)=\begin{cases} -\pi, & \text{if } x<-x_{b1}, \\ \pi x/x_{b1}, & \text{if } x_{b1}>x>-x_{b1}, \\ \pi, & \text{if } x>x_{b1}; \end{cases}$$

$\epsilon_f(=0.3)$ and $x_{b1}(=5x_b/6)$ are the profile control parameters of the driving electric field. In order to examine the influence of the spatial profile of $E_{d0}(x,t)$ on the simulation results, we carried out a test run for the case of $\epsilon_f=0.95$. By comparing the simulation result with that for the case of $\epsilon_f=0.3$, it is found that the fundamental properties of magnetic reconnection such as the growth rate and the saturation value of the reconnection electric field are hardly affected by the profile parameter ϵ_f.

In the previous paper[19] it is pointed out that the electron current layer becomes as thin as the average orbit amplitude of meandering electrons, which is three times larger than the grid separation. However, this value is close to the lower limit of the spatial resolution in the numerical calculation. This means that the numerical scheme with a higher spatial resolution than the previous one is required to obtain more physically comprehensive and reliable numerical results. Thus, we extend the semi-implicit EM simulation code used in the previous study to the explicit EM simulation code,[30] which has typically a ten times higher spatial resolution than the semi-implicit one. Because both electrons and ions are treated as particles in this method, a finite electron Larmor radius effect can be described as well as a finite ion Larmor radius effect and a particle inertia effect.

The ratio of the side lengths of the simulation box x_b/y_b is fixed to 3. This value is chosen so that the divergent plasma flow created at the reconnection point cannot arrive at the boundary of the x axis before the reconnection electric field reaches its maximum value. Therefore, it is possible to obtain the simulation results not affected by the boundary condition of the x axis as far as the initial dynamical phase is concerned. For the present simulation, 1 600 000 particles are used. The simulation domain is implemented on a (256 $\times$128) point grid. The side length of the simulation area along the y axis, $2y_b$, is nearly equal to $5\rho_{xi}$, which is four times smaller than the value used in the previous study[19] (ρ_{xi} is the ion Larmor radius associated with the asymptotic in-plane field B_0). The difference comes from the fact that the grid separation is determined by the Debye length in the explicit scheme while it can be much larger than the Debye length in the semi-implicit scheme. The time-step width Δt is determined so as to satisfy the Courant–Friedrichs–Lewy condition[31] for the electromagnetic wave in vacuum; the relation $\Delta t=0.5\Delta y/c$ holds in the present simulation where Δy $(=0.7\lambda_D)$ is the grid separation along the y axis and λ_D is the Debye length associated with an average number density at $t=0$.

III. SIMULATION RESULTS

We carry out six simulation runs with different values of initial longitudinal magnetic field B_{z0}. The simulation starts from the equilibrium profile the scale height of which is comparable to the ion Larmor radius ρ_{xi}, i.e., $L\approx 51\Delta y$, $\rho_{xi}\approx 25\Delta y$. The simulation is terminated before the divergent plasma flow created at the reconnection point arrives at the boundary of the x axis. The value of L is about one-half of the previous one[19] because of the difference in the simulation area size. Other typical parameters are as follows: the ratio of ion to electron mass M_i/M_e is 25, the maximum value of driving electric field E_0 is $-0.04B_0$, $\omega_{pe}/\omega_{ce}=3.5$, $c/(\omega_{pe}\Delta y)\approx 12$, and $\omega_{ce}\Delta t\approx 0.01$, where $\omega_{ce}(=eB_0/M_ec)$ is the electron cyclotron frequency. The relation $L>\rho_{xi}>c/\omega_{pe}>\Delta y$ holds in the initial profile for all cases.

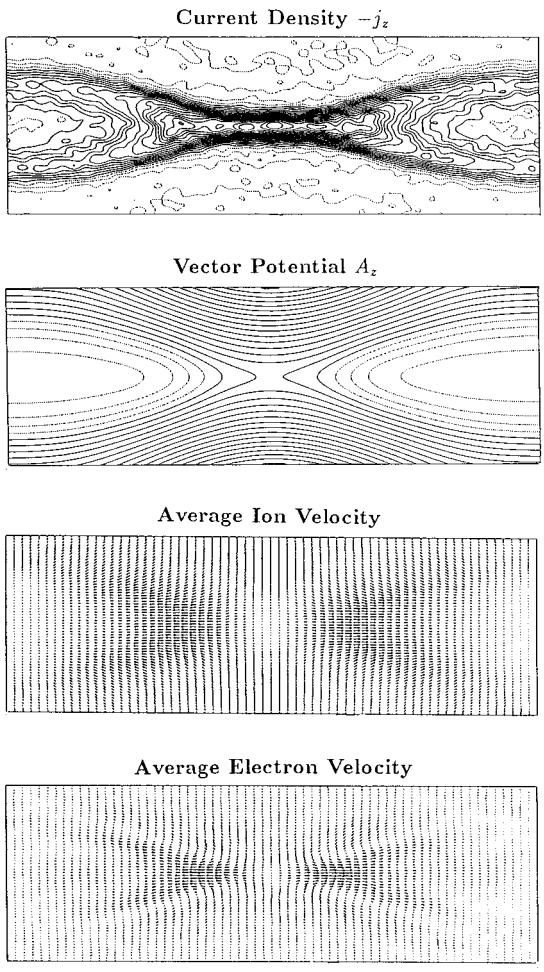

FIG. 1. Contour plots of the current density $-j_z$ (top), those of the vector potential A_z (second), the vector plots of the average ion velocity (third), and those of the average electron velocity (bottom) in the (x,y) plane at $\omega_{ce}t=100$ for the case of $B_{z0}=0$ where the current density contours less than the average value and the vector potential contours less than the initial value at the input boundary are plotted by dotted lines.

A. Fundamental properties of collisionless driven reconnection

In this section we examine the fundamental properties of collisionless driven reconnection by comparing the simulation results for the case of $B_{z0}=0$ with those obtained from the semi-implicit particle simulation.[19] Figure 1 shows the contour plots of the current density $-j_z$ (top), those of the vector potential A_z (second), the vector plots of the average ion velocity (third), and those of the average electron velocity (bottom) in the (x,y) plane at $\omega_{ce}t=100$ where the cur-

rent density contours less than the average value and the vector potential contours less than the initial value at the input boundary are plotted by dotted lines. The current density profile becomes peaked at the midpoint of the simulation domain because the plasma flow supplied through the boundary has a maximum input velocity at the midpoint of the input boundary ($x=0$, $y=\pm y_b$). An x-shaped structure of magnetic separatrix becomes visible as a result of magnetic reconnection. A fast directed flow arises from the x point after magnetic reconnection sets in and it carries the reconnected flux toward the boundaries of the x axis. The current density profile becomes elongated along the x axis by the divergent plasma flow and its spatial scale reaches about one-half of the x-side length of the simulation box. It is interesting to note that a clear x-shaped shock structure appears in the electron flow pattern while the ion flow pattern looks relatively faint due to the finite ion Larmor radius effect. The maximum value of the electron average velocity is about three times as large as that of the ion average velocity. This means that the net electric current appears in the (x,y) plane as a result of magnetic reconnection.

Figure 2 shows (a) the temporal evolution of the reconnection electric field $E_z^{(1)}$, (b) the temporal evolutions of four spatial scales, and (c) those of the electron number density (dotted line) and the ion number density (solid line) at the reconnection point where d_{Bx}, $d_{\rm skin}=c/\omega_{pe}$, l_{mi}, and l_{me} in Fig. 2(b) are the scale height of magnetic field B_x along the y axis, the electron skin depth associated with the electron number density inside the current layer, the average orbit amplitude of meandering ions and that of meandering electrons, respectively. The average amplitude of meandering motion is estimated by the particle temperature and the longitudinal magnetic field B_z averaged over the current layer and the in-plane magnetic field B_x just outside the current layer. It is clear from Fig. 2 that there are two temporal phases in the evolution of the reconnection field, i.e., the slow reconnection phase for $0<\omega_{ce}t<80$ and the fast reconnection phase for $80<\omega_{ce}t<100$. The growth rate is estimated to be $\gamma_1\approx 0.03\omega_{ce}$ for the slow reconnection phase and $\gamma_2\approx 0.07\omega_{ce}$ for the fast reconnection phase. These values are a few times as large as those of the semi-implicit study. This difference may come from the fact that the width of the initial current layer d_{Bx} is comparable to the average orbit amplitude of a meandering ion l_{mi} for the present case, while the width is about two times as large as the average orbit amplitude of meandering ions for the previous case. In other words, this suggests that the growth rate of the reconnection field strongly depends on the width of the current layer. The fact that the scale height d_{Bx} is comparable to l_{mi} in the first-half of the slow reconnection phase means that a finite ion Larmor radius effect becomes active in the current layer even at the starting period of the simulation. This is deeply connected with the phenomenon that the reconnection field grows slowly as soon as the simulation starts. The number densities at the center of the current layer increase due to the compression by the convergent plasma flow as time goes on, while the scale height d_{Bx} decreases and the current layer becomes narrower and narrower.

The width of the current layer approaches the average

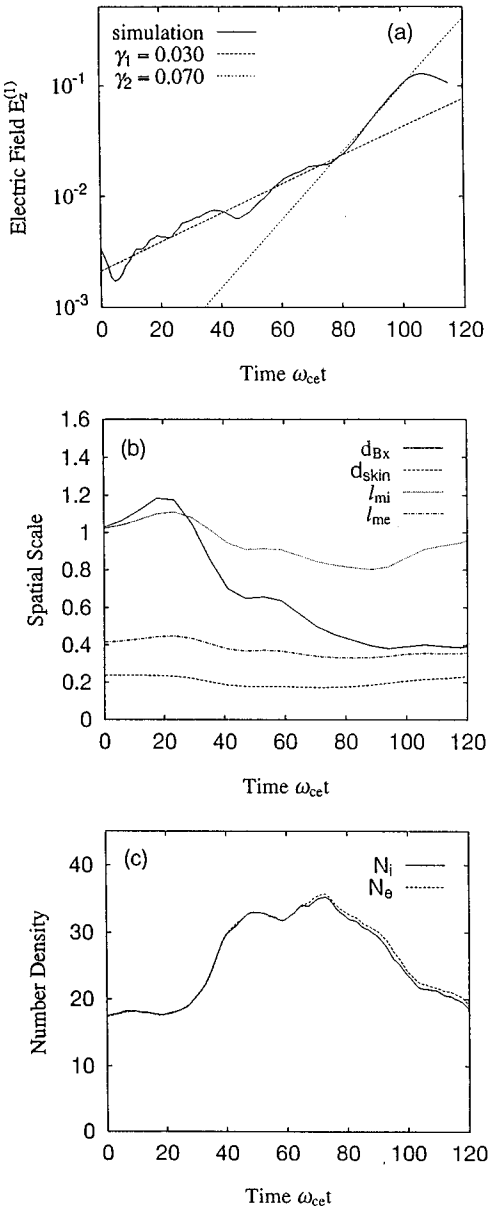

FIG. 2. Temporal evolutions of (a) the reconnection electric field $E_z^{(1)}$, (b) four spatial scales, and (c) the electron number density (dotted line) and the ion number density (solid line) at the reconnection point for the same case as Fig. 1. Here d_{Bx}, $d_{\rm skin}=c/\omega_{pe}$, l_{mt} and l_{me} in (b) are the scale height of magnetic field B_x, the electron skin depth, the average orbit amplitude of meandering ions and that of meandering electrons, respectively.

orbit amplitude of meandering electrons at the end of the slow reconnection phase. The fast reconnection phase starts after the number densities reaches the maximum value at $\omega_{ce}t\approx 70$. It is observable in Fig. 2(c) that the electron density becomes slightly dominant over the the ion number density in the fast phase. The violation of charge neutrality condition leads to the fast growth of electrostatic field in the current layer (electron current layer). This is because an electron motion is more strongly restricted by the motion of the magnetic field compared with an ion motion due to the finite Larmor radius effect. These results are consistent with the results obtained from the semi-implicit particle study. It is worth noting that the width of the electron current layer in

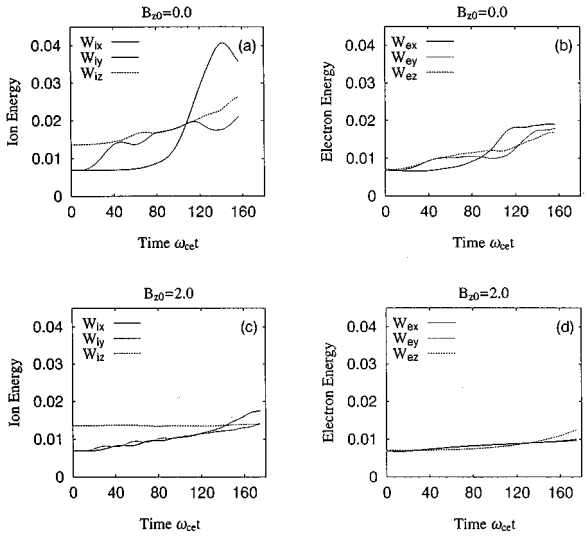

FIG. 3. Temporal evolutions of (a) the average ion energy for $B_{z0}=0$, (b) the average electron energy for $B_{z0}=0$, (c) the average ion energy for $B_{z0}=2B_0$, and (d) the average electron energy for $B_{z0}=2B_0$ where the solid, dotted, and dashed lines stand for the x component, the y component, and the z component of the energy per a particle averaged over the whole domain, respectively.

the fast reconnection phase is determined by the average orbit amplitude of electron meandering motion but not by the electron skin depth, i.e., the fast reconnection is triggered mainly by the electron meandering (thermal) effect but not by the electron skin depth (inertia) effect for this case.

B. Energy conversion by electric field

The reconnection electric field leads not only to the topological change of magnetic field lines but also to the energy conversion from the field energy to the particle energy through the acceleration and heating processes. Figure 3 shows (a) the temporal evolution of the average ion energy, (b) that of the average electron energy for the case of $B_{z0}=0$, (c) that of the average ion energy, (d) that of the average electron energy for the case of $B_{z0}=2B_0$, where the solid, dotted, and dashed lines stand for the x component, the y component, and the z component of the energy per particle averaged over the whole domain, respectively. The z component is larger than the other components by the energy of a diamagnetic motion at $t=0$.

Only the y component of the ion energy increases in the initial compression phase because the y component of the ion kinetic energy is dominant in the plasma flow supplied through the input boundary. This energy is transferred to the z component in a quarter of an ion gyration period ($\approx 40\omega_{ce}^{-1}$) because an ion gyrates in the (y,z) plane for $B_{z0}=0$. On the other hand, for the case of $B_{z0}=2B_0$, the ion energy of the input flow is transferred predominantly to the x component because an ion gyrates almost in the (x,y) plane due to the strong B_z field.

For the case of $B_{z0}=0$, both the x component of the ion energy and that of the electron energy increase rapidly after the reconnection electric field becomes maximum ($t=100\omega_{ce}^{-1}$). The time used for the energy conversion from the field energy to the ion energy is relatively longer compared with that to the electron energy. The saturation value of the ion energy becomes two times as large as that of the electron energy. The energy conversion occurs more actively in the plasma without any longitudinal magnetic field. This result is in good agreement with that of the plasma merging experiments done by Ono *et al.*[5] These differences come from the nature of the energy conversion mechanism in the presence of the electric field, as will be discussed in the following text.

Because the temporal change of the total field energy is described by

$$\frac{d}{dt}\int d^3x\left\{\frac{\mathbf{B}^2}{8\pi}+\frac{\mathbf{E}^2}{8\pi}\right\}=\int d^3x\left\{\boldsymbol{\nabla}\cdot\left(\frac{\mathbf{B}\times\mathbf{E}}{4\pi}\right)-\mathbf{E}\cdot\mathbf{j}\right\}, \tag{15}$$

the energy conversion between the field and the particles in the plasma is carried out through the work done by the electric field, i.e., the term $\mathbf{E}\cdot\mathbf{j}$. In order to obtain detailed information of this conversion process, let us decompose the electric field and the electric current as

$$\mathbf{E}=\mathbf{E}_{\mathrm{st}}+\mathbf{E}_{\mathrm{mg}}, \tag{16}$$

$$\mathbf{j}=\mathbf{j}_i+\mathbf{j}_e, \tag{17}$$

where $\mathbf{E}_{\mathrm{st}}$, $\mathbf{E}_{\mathrm{mg}}$, $\mathbf{j}_i$, and $\mathbf{j}_e$ are the electrostatic component, the electromagnetic component, the ion current, and the electron current, respectively. Figure 4 shows the color-coded contour maps of the energy conversion rates $\mathbf{E}_{\mathrm{mg}}\cdot\mathbf{j}_i$ (top), $\mathbf{E}_{\mathrm{st}}\cdot\mathbf{j}_i$ (second), $\mathbf{E}_{\mathrm{mg}}\cdot\mathbf{j}_e$ (third), and $\mathbf{E}_{\mathrm{st}}\cdot\mathbf{j}_e$ (bottom) in the (x,y) plane for the case of $B_{z0}=0$ where $\mathbf{E}_{\mathrm{mg}}\cdot\mathbf{j}_i$, $\mathbf{E}_{\mathrm{st}}\cdot\mathbf{j}_i$, $\mathbf{E}_{\mathrm{mg}}\cdot\mathbf{j}_e$, and $\mathbf{E}_{\mathrm{st}}\cdot\mathbf{j}_e$ stand for the energy conversion rate to the ion energy by the electromagnetic component, that to the ion energy by the electrostatic component, that to the electron energy by the electromagnetic component, and that to the electron energy by the electrostatic component, respectively. The red and blue colors in Fig. 4 stand for the positive and negative rates, respectively. For example, the bottom panel shows that the energy is converted from the particle to the field. There are two spatial regions in which the energy conversion occurs actively, i.e., the vicinity of the reconnection point and the shock-like region in the downstream. The electromagnetic component $\mathbf{E}_{\mathrm{mg}}$, which is dominated by the reconnection field E_z, acts on the particles in the vicinity of the reconnection point and leads mainly to the increase of the electron energy.

On the other hand, the electrostatic field $\mathbf{E}_{\mathrm{st}}$, which has only the x and y components, becomes significant at the shock-like region in the downstream, and it leads to the rapid increase of the ion energy and the decrease of the electron energy. The mechanism is as follows. Magnetic reconnection leads to the topological change of magnetic field as well as the electron acceleration along the z axis in the vicinity of the reconnection point. In other words, both the transverse component of the magnetic field B_y and the strong electron current j_z are generated as a result of magnetic reconnection. When an electron moves outside the narrow reconnection area, it becomes magnetized to be accelerated along the x axis by the resultant $\mathbf{j}\times\mathbf{B}$ force. The electron acceleration

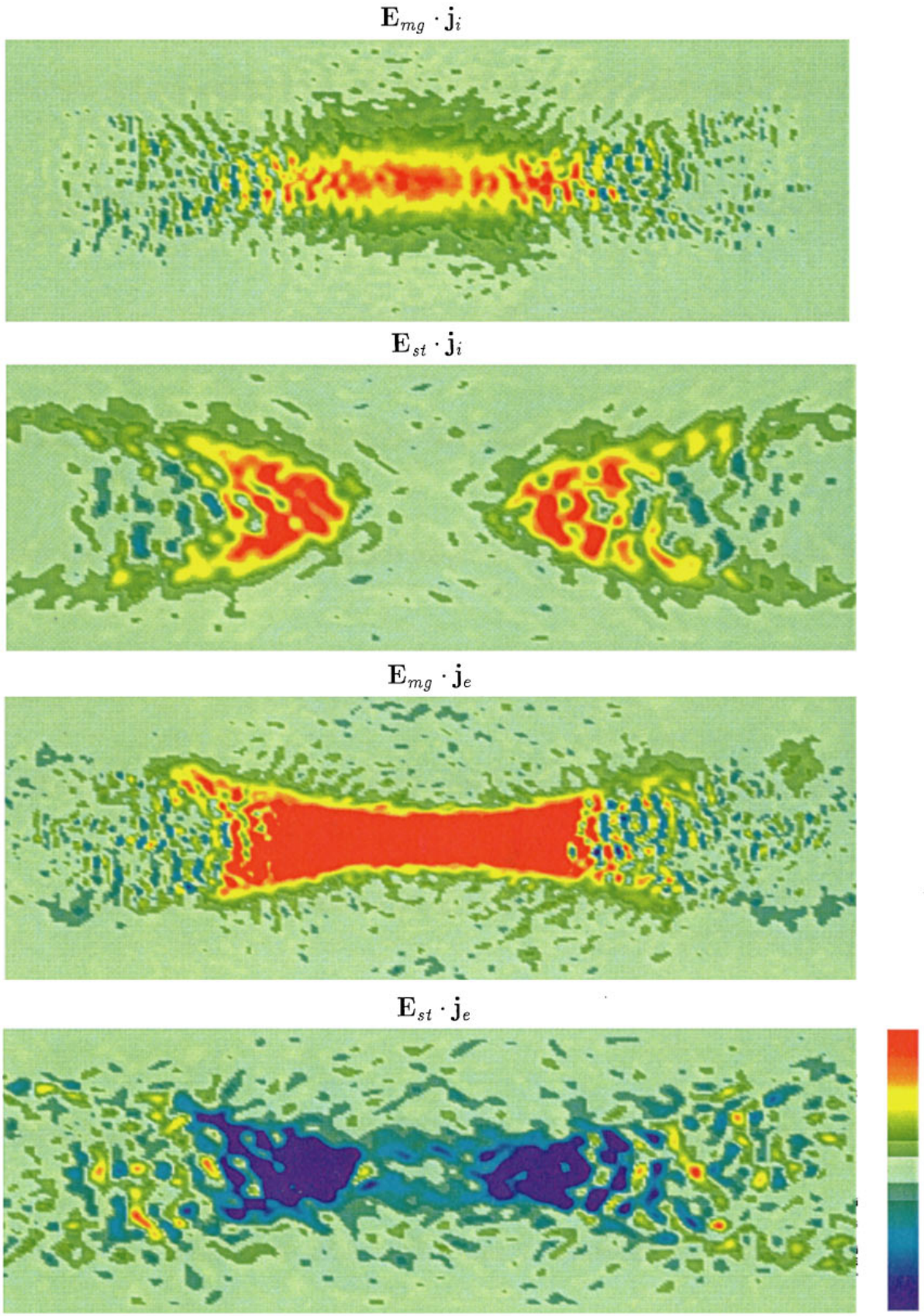

FIG. 4. The color-coded contour maps of the energy conversion rates $\mathbf{E}_{mg}\cdot\mathbf{j}_i$ (top), $\mathbf{E}_{st}\cdot\mathbf{j}_i$ (second), $\mathbf{E}_{mg}\cdot\mathbf{j}_e$ (third), and $\mathbf{E}_{st}\cdot\mathbf{j}_e$ (bottom) in the (x,y) plane for the same case as Fig. 1 where the red and blue colors stand for the positive and negative rates, respectively.

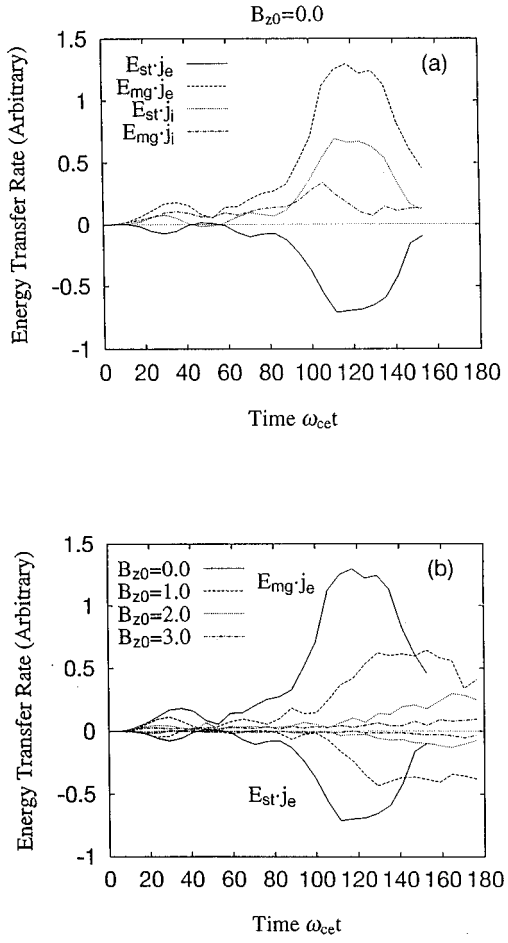

FIG. 5. Temporal evolutions of (a) four components of the total energy conversion rate between the field and particles for $B_{z0}=0.0$, and (b) the total conversion rates from the field to the electrons for four different longitudinal fields.

becomes so strong that the average electron velocity in the downstream is much larger than the average ion velocity (see Fig. 1) and the net electric current along the x axis appears in the downstream. The mass density profile is dynamically compressed by the magnetic flux which is carried by the divergent plasma flow. The electrostatic field is strongly generated in the region with steep density gradient due to the finite Larmor radius effect. This electrostatic field, in turn, works on decelerating the electron flow and accelerating the ion flow in the downstream, that is to say, the ambipolar interaction by the electrostatic field leads to the fast energy conversion from the electron energy to the ion energy in the downstream. It is important to note that, in the vicinity of the reconnection point, the energy conversion rate by the electrostatic field is negligibly small compared with that by the electromagnetic component. In other words, the electrostatic field does not play a leading role on either the particle acceleration or the thermalization in the vicinity of the reconnection point.

Let us examine the temporal behavior of the energy conversion rate and the influence of longitudinal magnetic field. Figure 5 shows (a) the temporal evolutions of the total conversion rates for the case of $B_{z0}=0.0$, and (b) the dependence of total conversion rates from the field energy to the electron energy on the longitudinal field B_{z0}, where the total rate is obtained by integrating over the whole simulation area. Although the total conversion rate varies with time and the longitudinal field, both the electromagnetic and electrostatic components always work on the particles in the same way. That is, the energy is monotonously converted from the electromagnetic field to the ions. On the other hand, the electrons always get the energy through the action of the reconnection field and lose it under the influence of the electrostatic field in the downstream irrespective of the values of B_{z0}. These facts explain why the ion energy increases twice as much as the electron energy (see Fig. 3). Furthermore, we can find an interesting feature in Fig. 5(a), namely, that two conversion rates by the electrostatic field, $\mathbf{E}_{\rm st}\cdot\mathbf{j}_i$ (dotted curve) and $\mathbf{E}_{\rm st}\cdot\mathbf{j}_e$ (solid curve), reveal very similar behaviors except for the fact that the ion rate is always positive and the electron rate is always negative. This is additional evidence that the electrostatic (ambipolar) field excited in the downstream acts as an energy conversion channel from the electrons to the ions in a collisionless plasma. It is clearly observed in Fig. 5(b) that the energy conversion becomes less effective as B_{z0} increases, as was seen in Fig. 3.

C. Particle acceleration and heating

In this section, we examine the energy conversion process along the particle trajectory for the case of $B_{z0}=0$. For this purpose we mark about 6000 electrons and ions which exist in the vicinity of the reconnection point at the period of $\omega_{ce}t=100$ when the reconnection electric field reaches its maximum value. The distribution function of marked electrons is shown in Fig. 6 as a function of v_z where the top, middle and bottom panels represent the distribution functions at $\omega_{ce}t=82$, 100, and 118, respectively. We can observe that the electron distribution shifts toward the positive v_z direction as a whole, while making its profile broader when the electrons pass across the reconnection area ($\omega_{ce}t=100$). That is, the electron heating and acceleration along the z axis take place simultaneously. Most of the electron average momentum along the z axis is lost and the distribution becomes even broader at $\omega_{ce}t=118$ when the electrons move in the downstream.

Let us examine the particle heating and acceleration process in more detail. Figure 7 shows (a) the temporal evolutions of the average velocity, the thermal velocity, and the average vector potential A_z of the marked electrons, (b) those of the marked ions, and (c) the temporal evolution of four energy conversion rates evaluated at particle positions, $-\mathbf{E}_{\rm st}\cdot\mathbf{u}_e$, $-\mathbf{E}_{\rm mg}\cdot\mathbf{u}_e$, $\mathbf{E}_{\rm st}\cdot\mathbf{u}_t$, and $\mathbf{E}_{\rm mg}\cdot\mathbf{u}_t$. The spatial position of marked particles is expressed in terms of the normalized vector potential, which is unit at the input boundary, zero at the reconnection point, and negative in the downstream. The x and y components of the average particle velocity in Figs. 7(a) and 7(b), u_x and u_y, are illustrated so as to be negative for the convergent flow and positive for the divergent flow.

The electron acceleration and thermalization along the z direction take place rapidly as soon as they enter into the reconnection area, as was seen in Fig. 6. The time scale of electron acceleration and thermalization is estimated to be about $10/\omega_{ce}$, which is in good agreement with the time τ_e

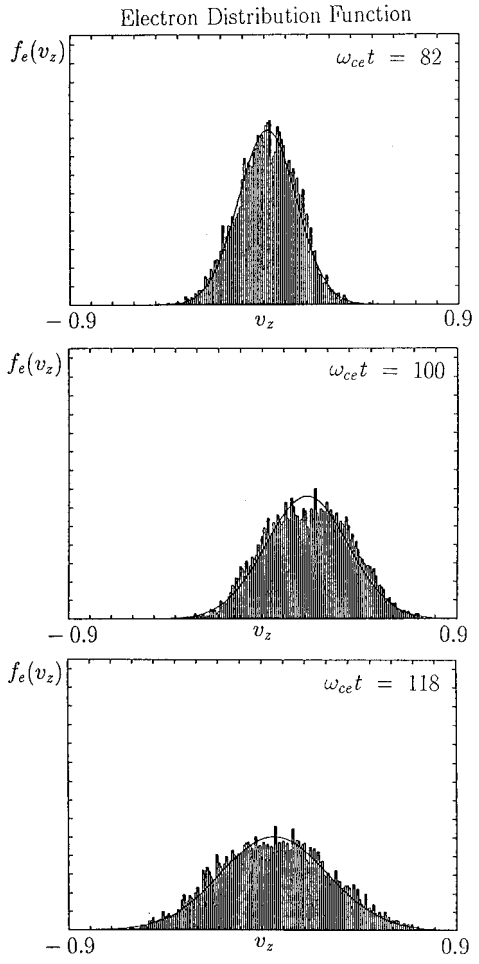

FIG. 6. Distribution functions of about 6000 marked electrons at $\omega_{ce}t=82$ (top), 100 (middle), and 118 (bottom) for the same case as Fig. 1.

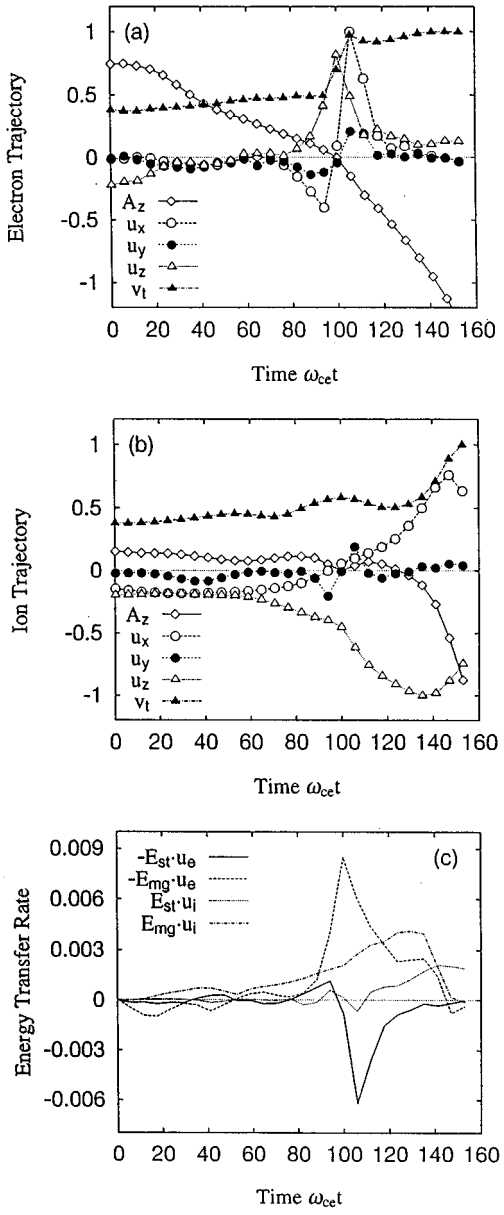

FIG. 7. Temporal evolutions of (a) the average velocity, the thermal velocity, and the average vector potential A_z of the marked electrons, (b) those of the marked ions, and (c) four energy conversion rates evaluated at particle positions for the same case as Fig. 1.

needed for a thermal electron to pass through the electron current layer, i.e., $\tau_e=2l_{me}/v_{te}$. This agreement also implies that both the electron acceleration and thermalization processes become active when the electrons exist in the reconnection area defined by the width of the electron current layer. The reconnection area corresponds to the diffusion area in the fluid model. The behavior of u_x in Fig. 7(a) exhibits that the electron flow changes from the convergent type ($u_x<0$) to the divergent type ($u_x>0$) when they pass across the reconnection point ($A_z=0$). The transverse (y) component of the magnetic field is created as a result of magnetic reconnection. The fast electron motion toward the downstream sides along the x axis is generated mainly by the resultant $\mathbf{j}_e\times\mathbf{B}$ force. The electron motion is gradually decelerated by the electrostatic field in the downstream as the electrons move from the vicinity of the reconnection point to the downstream sides. Thus, the average electron velocity vanishes in the downstream. In contrast to this, the electron thermal velocity remains almost constant in the downstream.

Because the unmagnetized region for ions is wider and the ion thermal velocity is lower compared with those for electrons, thermal ions remain in the reconnection area for a relatively long period. The time τ_i needed for a thermal ion to pass through the reconnection area is estimated to be about $30/\omega_{ce}$. As $\tau_i \gg \tau_e$, the ions are accelerated along the z axis for a relatively long period by the reconnection electric field when they pass across the vicinity of the reconnection point. The z component of the ion average velocity becomes about 2.0 of the initial Alfvén velocity v_{A0} when the ions go outside the reconnection area. On the other hand, there is no significant change in the thermal velocity when the ions pass through the reconnection area. One can find that the ions are thermalized more effectively by the electrostatic field when they move in the downstream ($t>130\omega_{ce}$) than when they exist inside the reconnection area ($t<130\omega_{ce}$). Thus, it is concluded that the electron heating takes place in the reconnection area under the influence of the reconnection electric field while the ion heating takes place in the downstream by the action of the electrostatic field.

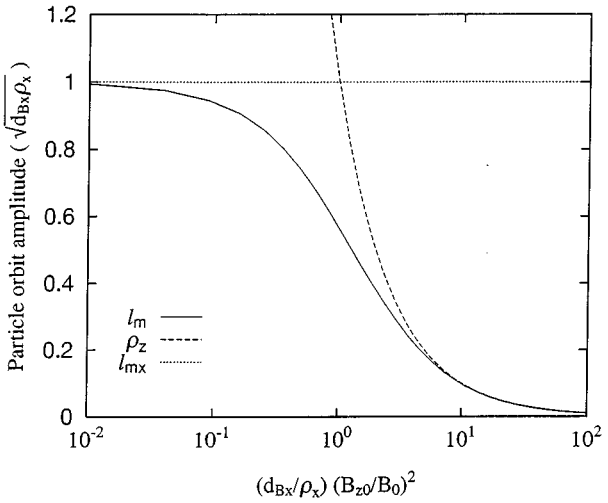

FIG. 8. Orbit amplitude of a test particle in a one-dimensional sheared magnetic field where l_m, l_{mx}, ρ_x and ρ_z are an orbit amplitude in a sheared field, that for $B_{z0}=0.0$, the Larmor radius associated with an in-plane field B_0, and that associated with a longitudinal field B_{z0}, respectively.

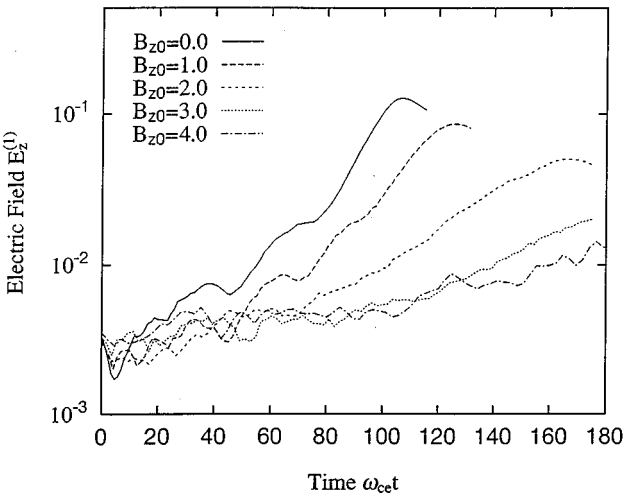

FIG. 9. Temporal evolution of the reconnection electric field for five different values of B_{z0}.

D. Reconnection mechanism

It has so far been pointed out that there exist two mechanisms associated with microscale particle effects which lead to magnetic reconnection in a collisionless plasma. One is a particle inertia effect which becomes significant in a spatial scale comparable to collisionless skin depth c/ω_p. The other is a particle orbit effect which becomes effective in a characteristic spatial scale of particle meandering motion. We have observed that magnetic reconnection is controlled by a meandering orbit effect for the case of $B_{z0}=0$ where an average orbit amplitude of meandering electrons is larger than an electron skin depth in the current layer. The average orbit amplitude of meandering motion in the current layer becomes shorter and so a charged particle becomes more strongly magnetized as the longitudinal magnetic field becomes stronger, as is shown in Fig. 8. Because collisionless driven reconnection is deeply connected with the meandering motion of charged particles in the current layer, it is natural to expect that both the magnetic reconnection and energy conversion processes are largely affected by longitudinal magnetic field.

First, let us examine the influence of the longitudinal field on the behavior of the reconnection electric field. The temporal evolution of the reconnection electric field is shown in Fig. 9 for five different values of B_{z0}. Careful examination of Fig. 9 reveals that there exist both the slow reconnection phase and the fast reconnection phase irrespective of longitudinal field. However, both the growth rate and the saturation value of the reconnection electric field decrease as the longitudinal field becomes stronger. The same feature was observed in the plasma merging experiments[4] which investigated the three-dimensional effect of magnetic reconnection by use of axially colliding spheromaks. The growth rate for the slow phase γ_1 and that for the fast phase γ_2 are shown in Fig. 10 as a function of B_{z0}/B_0, where the maximum $\mathbf{E}\times\mathbf{B}$ drift velocity at the input boundary, $v_{\text{in}}=v_{n0}/\{1+(B_{z0}/B_0)^2\}^{1/2}$ (v_{n0} is constant), is added for comparison. One can find that both the growth rates, γ_1 and γ_2, reveal very similar behavior to the input plasma velocity v_{in}. Because the maximum input rate of the in-plane magnetic flux is approximately given by $E_0/\{1+(B_{z0}/B_0)^2\}^{1/2}$, this result implies that the growth of the reconnection electric field is controlled by the input rate of the in-plane magnetic flux at the boundary. In other words, the whole dynamical behavior of collisionless driven reconnection is determined by the external condition, such as a flux input rate into the system, even if magnetic reconnection would be triggered by a microscale electron mechanism in the central region of current layer. In this sense, this result is also in good agreement with the result of the semi-implicit study.[19]

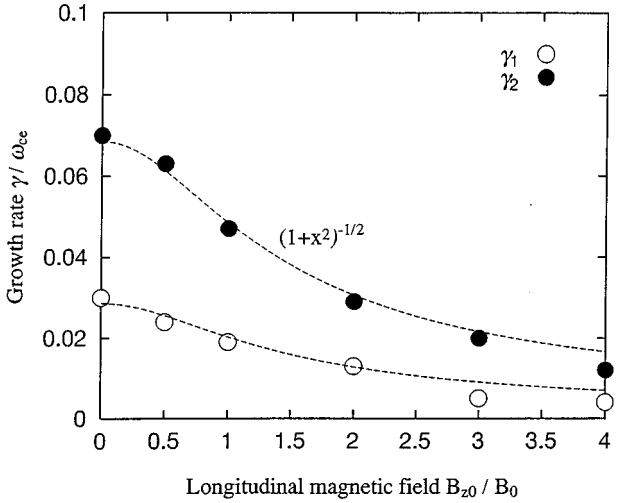

FIG. 10. The dependence of growth rates of reconnection electric field on the field ratio B_{z0}/B_0 where the open and closed circles show the growth rate for the slow phase γ_1 and that for the fast phase γ_2, respectively. The maximum $\mathbf{E}\times\mathbf{B}$ drift velocity at the input boundary is illustrated by a dashed line for comparison.

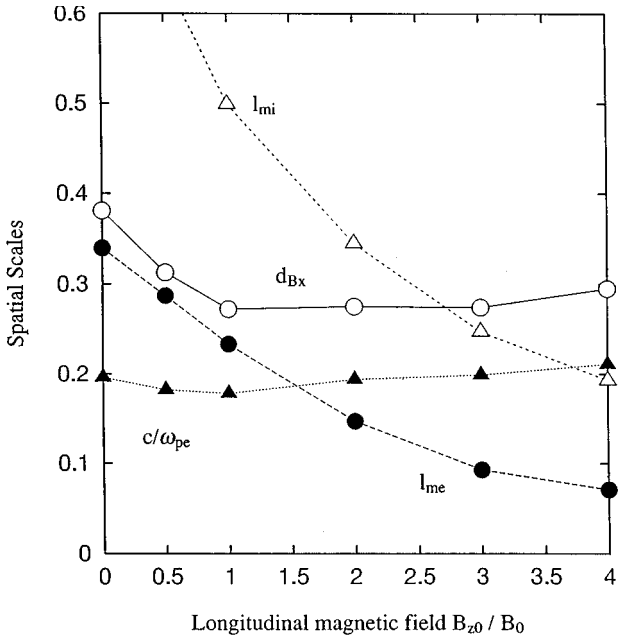

FIG. 11. The dependence of four spatial scales on the field ratio B_{z0}/B_0 where the scales are estimated at the period when the current layer becomes thinnest.

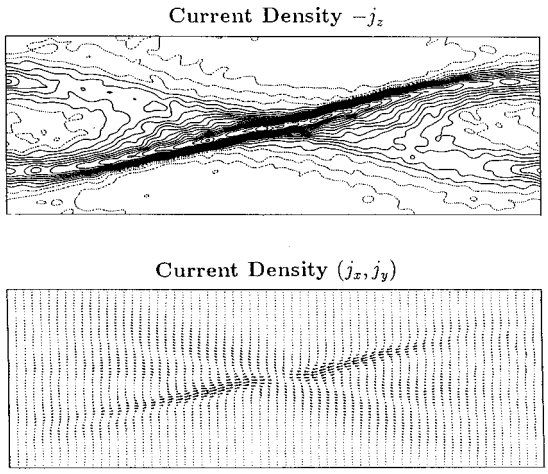

FIG. 12. Contour plots of the z component of current density (top) and the vector plots in the (x,y) plane (bottom) at $\omega_{ce}t=118$ for the case of $B_{z0}=B_0$.

Now let us turn to the triggering mechanism of collisionless driven reconnection in the fast phase. In this phase the current layer is compressed so thin that a microscale electron effect becomes visible and magnetic flux inside the current layer is no longer frozen in the electron fluid. Figure 11 illustrates the dependence of four spatial scales on the field ratio B_{z0}/B_0 when the current layer becomes thinnest in the fast reconnection phase. For the case of $B_{z0}=0$, the width is nearly equal to the average orbit amplitude of meandering electrons l_{me}, which is about two times as large as the electron skin depth c/ω_{pe} [see also Fig. 2(b)]. The average orbit amplitude l_{me} decreases as the longitudinal field increases. This corresponds to the fact that the unmagnetized region for electrons becomes narrower with the longitudinal field, as was seen in Fig. 8. On the other hand, the electron skin depth increases slightly with B_{z0}/B_0 because the plasma becomes less compressible and the increase of plasma density in the current layer is suppressed by the longitudinal field for $B_{z0} \gg B_0$. Thus, the relation $l_{me} < c/\omega_{pe}$ holds for the strong longitudinal field of $B_{z0} > 1.5B_0$. In other words, the electron inertia scale is longer than the electron thermal scale for $B_{z0} > 1.5B_0$. It is clearly seen in Fig. 11 that the width of the current layer decreases with the electron thermal scale l_{me} until l_{me} reaches c/ω_{pe}. When $l_{me} < c/\omega_{pe}$, the width ceases to decease and exhibits the same behavior with the electron skin depth. Namely, collisionless driven reconnection in the fast reconnection phase proceeds, keeping the width of the current layer nearly equal to the electron skin depth for the strong longitudinal field of $B_{z0} > 1.5B_0$. These results lead us to the conclusion that the triggering mechanism for collisionless driven reconnection in the fast reconnection phase changes from the electron thermal effect to the electron inertia effect in accordance with the increase of longitudinal magnetic field.

E. Asymmetric current profile

A longitudinal field has an influence on the physical processes responsible for collisionless driven reconnection, i.e., the plasma compressibility, the magnetization of a charged particle, the reconnection rate, and so on. In this section we present another phenomenon which appears under the influence of the longitudinal field. The reconnection electric field accelerates the charged particles in the direction normal to the reconnection magnetic field, i.e., in the z direction. If the z component of the magnetic field is nonzero, the acceleration by the reconnection field creates the electric current flowing parallel to the magnetic field. Let us consider the influence of the parallel electric current on the collisionless reconnection process. Figure 12 shows the contour plots of the z component of current density (top) and the vector plots in the (x,y) plane (bottom) at $\omega_{ce}t=118$ for the case of $B_{z0}=B_0$. Comparing Fig. 12 with Fig. 1 one can find that the spatial structure of the current layer becomes longer and asymmetric by adding the longitudinal magnetic field.

Let us consider the mechanism leading to the asymmetric current profile. For the case of $B_{z0}=0$, the straight elongated current layer is formed as a result of magnetic reconnection, as was seen in Fig. 1. A fast divergent electron flow along the x axis in the current layer carries the net electric current because the average electron velocity is about three times as large as the average ion velocity. The resultant $\mathbf{j}\times\mathbf{B}$ force, in turn, acts on the electron in the negative z direction ($j_x B_y < 0$) while the average electron motion carrying the equilibrium current directs to the positive z direction ($u_{ez} > 0$). Consequently, the average electron velocity along the z axis is gradually lost as the fast electron flow moves toward the downstream. In this process there exists no force which modifies the current layer in an asymmetric form. Thus, the elongated current layer is terminated in the downstream and its shape is maintained symmetric with respect to the mid-horizontal line for the case of $B_{z0}=0$.

Suppose that the longitudinal magnetic field of $B_{z0} \gg B_0$ is superposed on this symmetric profile. The $\mathbf{j}\times\mathbf{B}$ force associated with the longitudinal field and the electron current

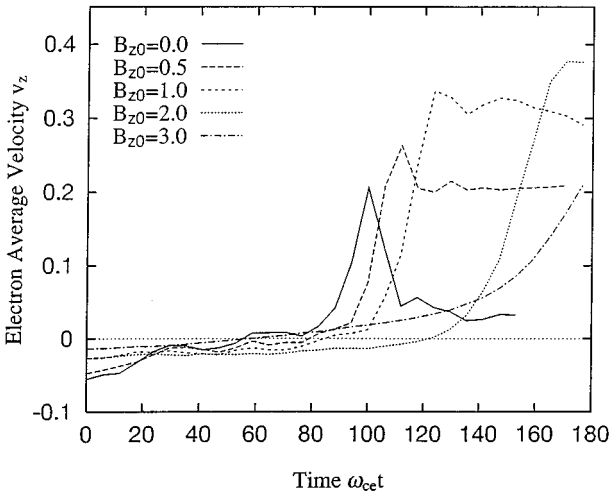

FIG. 13. Temporal evolutions of the average electron velocity along the z axis for five different values of B_{z0} where the average is carried out over about 6000 electrons which pass across the vicinity of the reconnection point when the reconnection electric field reaches its maximum value.

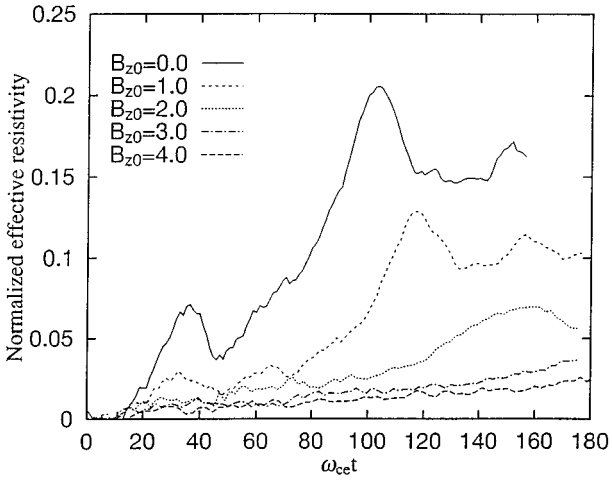

FIG. 14. Temporal evolution of the effective resistivity for five different values of B_{z0} where the resistivity is normalized by the Hall resistivity B_0/qcn_e.

along the x axis is in the negative y direction for the left-half of the simulation plane ($x<0$) and in the positive y direction for the right-half of the simulation plane ($x>0$). When the electron moves halfway in the current layer along the x axis, the effect of the $\mathbf{j}\times\mathbf{B}$ force is visible in the electron current profile. The bending of the current layer proceeds so that the electron current becomes parallel to the magnetic field, i.e., the force-free condition is satisfied between the electric current and the magnetic field. Therefore, the parallel current enhanced by the reconnection field is maintained for a long period when the fast plasma flow moves in the bent current layer at the downstream.

We have another piece of evidence that the force-free current is maintained for a long period in the downstream in the presence of longitudinal field. Figure 13 shows the temporal evolutions of the average velocity along the z axis for about 6000 marked electrons which pass across the vicinity of the reconnection point when the reconnection electric field reaches its maximum value. The electrons are accelerated by the reconnection electric field when they exist in the reconnection area. The force-free current generated through the acceleration by the reconnection field is maintained for a long period in the downstream in the presence of the longitudinal field, while, for the case of $B_{z0}=0$, the average electron momentum is immediately lost as soon as they move into the downstream. It is interesting to note that the maximum electron velocity increases with B_{z0} although the reconnection field decreases as B_{z0} increases (see Fig. 9). This implies that the existence of the longitudinal magnetic field makes it easy for the reconnection field to accelerate the electrons along the z axis. This phenomenon is also explained in terms of the effective resistivity η_{eff}, which is defined by the ratio of the electric field to the current density at the reconnection point, i.e., E_z/j_z. The temporal evolution of the effective resistivity is illustrated in Fig. 14 for five different values of B_{z0} where the resistivity is normalized by the Hall resistivity B_0/qcn_e. Figure 14 clearly shows that the effective resistivity varies roughly inversely proportional to B_{z0}. This means that the electric field needed for maintaining the electric current decreases as the longitudinal field increases. It is concluded that, under the influence of the longitudinal magnetic field, the electron acceleration by the reconnection field takes place effectively and the generated force-free current is maintained for a long period while forming an asymmetric spatial profile of current layer.

IV. SUMMARY AND DISCUSSIONS

We have investigated the nonlinear development of collisionless driven reconnection and the consequent energy conversion between particles and an electromagnetic field in a sheared magnetic field by making use of a two-and-one-half-dimensional particle simulation. The main results are summarized by the following remarks, labeled (A)–(F).

(A) The reconnection electric field evolves in two steps irrespective of the existence of a longitudinal magnetic field, i.e., (1) slow reconnection triggered by the ion kinetic effect in the early phase, and (2) fast reconnection triggered by the electron kinetic effect in the late phase. The existence of these two temporal phases is deeply connected with the formation of two types of current layer, i.e., electron current layer and ion current layer.

(B) The growth rate of the reconnection electric field and its saturation value are determined by the flux input rate at the boundary, but not by the detailed mechanism leading to collisionless reconnection in the current layer. This is an important feature which is commonly observed in the phenomena triggered by driven magnetic reconnection.[1]

(C) There are two microscopic particle effects which lead to collisionless magnetic reconnection in a two-dimensional system. For a weak longitudinal magnetic field case, the width of the electron current layer is determined by the average orbit amplitude of meandering electrons. As the longitudinal magnetic field

increases, thermal motion becomes more strongly magnetized and the orbit amplitude of meandering electrons becomes shorter. For a strong longitudinal field case where the electron skin depth is larger than the average orbit amplitude of meandering electrons, the inertia effect becomes dominant and the width of the electron current layer is determined by the electron skin depth.

(D) Electron acceleration and thermalization take place in the reconnection area under the influence of the reconnection electric field. On the other hand, the electrostatic field does not play a leading role on either the particle acceleration or the thermalization in the vicinity of the reconnection point.

(E) The electrostatic field, which is generated in the downstream as a result of magnetic compression by the divergent reconnection flow, acts as an energy conversion channel from the electrons to the ions in a collisionless plasma. Thus, the total ion energy becomes twice as large as the total electron energy. The energy conversion takes place more actively in the plasma without any longitudinal magnetic field and its rate decreases with the longitudinal field.

(F) The existence of the longitudinal magnetic field makes it easy for the electric field to accelerate electrons along the equilibrium current at the reconnection point and plays a role in maintaining the generated force-free current for a long period by forming an asymmetric spatial profile of current layer.

The plasma merging experiments[4,5] revealed that the reconnection rate and the energy conversion rate are strongly dependent on the reconnection angle between the merging field lines or the ratio of the longitudinal magnetic field to the in-plane field. This result is in good agreement with the simulation results in this paper. Since the existence of the longitudinal magnetic field makes a plasma less compressible, this result indicates that the plasma compressibility is a key factor in determining the behavior of driven reconnection. The anomalous ion heating is often observed in experimental plasmas[5,28] in which a MHD relaxation controlled by magnetic reconnection takes place. This paper may give an explanation of this phenomenon. That is, the ion heating takes place through the action of the electrostatic field generated in the downstream after the ions are accelerated by the electric field in the reconnection area.

In considering the whole physical process of collisionless driven reconnection, it is important to examine the dependence of the simulation results on simulation parameters such as ion mass, electron mass, the driving electric field, and so on. The semi-implicit study[19] examined the dependence on the ion mass, the electron mass, and the driving electric field, while the dependence on the longitudinal magnetic field has been examined in this paper. These studies disclosed that the fundamental properties of collisionless driven reconnection are determined by two physical processes, i.e., the external process which controls the flux input rate into the current layer, and the internal process which controls the particle kinetic mechanism leading to collisionless driven reconnection in the current layer. One of the important conclusions is that they are not independent processes but are deeply connected to each other. For example, collisionless driven reconnection proceeds so that the reconnection rate is balanced with the flux input rate into the current layer while changing the physical conditions such as the width of current layer, particle temperature, and magnetic field in the current layer.

We focus the discussions in this paper on the initial dynamical phase but not on the following saturation phase. This is because an exact steady state cannot be realized within the framework of this study due to the boundary conditions. That is, the total number of charged particles increases monotonously with time and the time derivative of the magnetic field B_y is always nonzero at the boundary because $\partial E_z/\partial x \neq 0$. Therefore, it is necessary to develop a new simulation code which can deal with a steady state problem in order to investigate collisionless driven reconnection in the saturation phase, especially its dependence on the boundary condition or the initial condition.

The present particle simulation study has clarified the particle kinetic effect in collisionless driven reconnection under the assumption that the spatial dependence along the equilibrium current can be ignored. The interaction between particles carrying electric current and a wave propagating along the electric current becomes an origin of an anomalous resistivity[22] which can also lead to collisionless reconnection. Three-dimensional treatment is needed for the investigation of this effect in collisionless driven reconnection and the relation between the particle kinetic effect and the effect of wave–particle interaction. This problem will be discussed elsewhere in the future.

ACKNOWLEDGMENTS

One of the authors (R.H.) is grateful to Professor S. Bazdenkov and Professor D. Biskamp for useful discussions. The simulation work was performed by employing the Advanced Computing System for Complexity Simulation at the National Institute for Fusion Science (NIFS).

This work was supported in part by Grants-in-Aid from the Ministry of Education, Science and Culture in Japan (Nos. 07832024, 08044109, and 08226104).

[1] T. Sato and T. Hayashi, Phys. Fluids **22**, 1189 (1979); T. Sato, T. Hayashi, K. Watanabe, R. Horiuchi, M. Tanaka, N. Sawairi, and K. Kusano, Phys. Fluids B **4**, 450 (1992).
[2] E. R. Priest, *Solar Magnetohydrodynamics* (Reidel, Dordrecht, 1982).
[3] A. Nishida, *Geomagnetic Diagnostics of the Magnetosphere* (Springer-Verlag, New York, 1978), p. 38.
[4] M. Yamada, Y. Ono, A. Hayakawa, M. Katsurai, and F. W. Perkins, Phys. Rev. Lett. **65**, 721 (1990); Y. Ono, A. Morita, M. Katsurai, and M. Yamada, Phys. Fluids B **5**, 3691 (1993).
[5] Y. Ono, M. Yamada, T. Akao, T. Tajima, and R. Matsumoto, Phys. Rev. Lett. **76**, 3328 (1996).
[6] T. Sato, Y. Nakayama, T. Hayashi, K. Watanabe, and R. Horiuchi, Phys. Rev. Lett. **63**, 528 (1989); R. Horiuchi and T. Sato, Phys. Fluids B **4**, 672 (1992).
[7] W. Horton and T. Tajima, Geophys. Res. Lett. **17**, 123 (1990).
[8] G. Laval, R. Pellat, and M. Vuillemin, *Plasma Physics and Controlled Fusion Research* (International Atomic Energy Agency, Vienna, 1966), Vol. II, p. 259.
[9] B. Coppi, G. Laval, and R. Pellat, Phys. Rev. Lett. **16**, 1207 (1966).
[10] K. Schinder, J. Geophys. Res. **79**, 2803 (1974).
[11] J. D. Drake and Y. C. Lee, Phys. Rev. Lett. **39**, 453 (1977).

[12]A. A. Galeev, *Basic Plasma Physics II* (North-Holland, New York, 1984), p. 305.
[13]X. Wang and A. Bhattacharjee, J. Geophys. Res. **98**, 19419 (1993).
[14]I. Katanuma and T. Kamimura, Phys. Fluids **23**, 2500 (1980).
[15]J. N. Leboeuf, T. Tajima, and J. M. Dawson, Phys. Fluids **25**, 784 (1982).
[16]D. W. Hewett, G. E. Frances, and C. E. Max, Phys. Rev. Lett. **61**, 893 (1988).
[17]W. Zwingmann, J. Wallance, K. Schindler, and J. Birn, J. Geophys. Res. **95**, 20877 (1990).
[18]P. L. Pritchett, F. V. Coroniti, R. Pellat, and H. Karimabadi, J. Geophys. Res. **96**, 11523 (1991).
[19]R. Horiuchi and T. Sato, Phys. Plasmas **1**, 3587 (1994).
[20]M. Ottaviani and F. Porcelli, Phys. Rev. Lett. **71**, 3802 (1993).
[21]D. Biskamp, E. Schwarz, and J. F. Drake, Phys. Rev. Lett. **75**, 3850 (1995); B. Rogers and L. Zakharov, Phys. Plasmas **3**, 2411 (1996).
[22]For example, R. C. Davidson and N. T. Gladd, Phys. Fluids **18**, 1327 (1975); P. C. Liewer and R. C. Davidson, Nucl. Fusion **17**, 85 (1977); A. A. Galeev and R. Z. Sagdeev, in Ref. 12, p. 271; M. Tanaka and T. Sato, J. Geophys. Res. **86**, 5541 (1981); M. Ozaki, T. Sato, R. Horiuchi, and the Complexity Simulation Group, Phys. Plasmas **3**, 2265 (1996).
[23]A. Fruchtman and K. Gomberoff, Phys. Fluids B **5**, 2371 (1993).
[24]R. Horiuchi and T. Sato, Phys. Fluids B **2**, 2652 (1990).
[25]Z. Yoshida and T. Uchida, Jpn. J. Appl. Phys. **34**, 4213 (1995).
[26]M. Tanaka and T. Sato, Phys. Fluids **29**, 3823 (1986).
[27]S. Murakami and T. Sato, J. Phys. Soc. Jpn. **61**, 849 (1992).
[28]T. Fujita, K. Saito, J. Matsui, Y. Kamada, H. Morimoto, Z. Yoshida, and N. Inoue, Nucl. Fusion **31**, 3 (1991).
[29]Z. Yoshida and A. Hasegawa, Phys. Fluids B **4**, 3013 (1992).
[30]C. K. Birdsall and A. B. Langdon, *Plasma Physics via Computer Simulation* (McGraw-Hill, New York, 1985), p. 351.
[31]R. Courant, K. O. Friedrichs, and H. Lewy, Math. Ann. **100**, 32 (1928).